Article

Carbon-Based Perovskite Solar Cell Enables Graded Utilization of Full Solar Spectrum Beyond the Photovoltaic S-Q Limit via Hybrid Photovoltaics–Photothermal Conversion

Kai Zhang [1,2,†], Chi Zhang [3,†], Zedong Lin [4,†], Changqing Lin [1,2], Xiaozhen Wei [1,2,5], Min Ju [3], Chunyu Lv [1,2,5], Haining Chen [5], Zhenhai Yang [6], Jian Wang [3,*], Weibiao Zhong [1,2], Qifeng Lin [1,2], Yi He [1,2] and Shihe Yang [1,2,*]

[1] School of Advanced Materials, Guangdong Provincial Laboratory for Nano-Micro Materials Research, Shenzhen Graduate School, Peking University, Shenzhen 518055, China
[2] Institute of Biomedical Engineering, Shenzhen Bay Laboratory, Shenzhen 518107, China
[3] School of Energy and Environment, City University of Hong Kong, Hong Kong SAR, China
[4] School of Materials Science and Engineering, Taizhou University, Taizhou 318000, China
[5] School of Materials Science and Engineering, Beihang University, Beijing 100191, China
[6] School of Optoelectronic Science and Engineering & Collaborative Innovation Center of Suzhou Nano Science and Technology, Soochow University, Suzhou 215006, China
* Correspondence: jian.wang@cityu.edu.hk (J.W.); chsyang@pku.edu.cn (S.Y.)
† These authors contributed equally to this work.

Abstract: The energy conversion efficiency of a single-junction photovoltaic device is mainly constrained by its bandgap setting a theoretical upper bound known as Shockley-Queisser (S-Q) limit. In this work, carbon-based perovskite solar cells (C-PSCs) are harnessed to transcend the S-Q limit through a synergistic integration of photovoltaic and photothermal conversion for water splitting: the above-bandgap photons are converted into electrical energy, while the below-bandgap photons are all transformed into thermal energy through the carbon composite electrode. Correlative investigations into photovoltaic performance under varying solar driven heat-accumulation conditions, irradiance spectra, and incident light intensity reveal that C-PSCs exhibit lower temperature coefficients and higher full-spectrum solar energy utilization than conventional silicon cells. Furthermore, we calculated the S-Q efficiency limits under varying temperatures, irradiation spectra, and bandgap configurations, thereby offering critical insights for optimizing graded utilization of full solar spectrum. By integrating C-PSCs with water-splitting electrolytic cells, a graded utilization of full solar spectrum through both photovoltaic and photothermal conversion within the single-junction device is achieved. This integration elevates the solar-to-hydrogen (STH) efficiency from 11.30% to 12.98%, representing an enhancement of 14.86%, and achieves a remarkable STH-to-power conversion efficiency (PCE) ratio of up to 71.0%, highlighting its profound transformative potential.

Keywords: Shockley-Queisser efficiency limit; graded utilization of full solar spectrum; carbon-based perovskite solar cells; photothermoelectrical coupling; photovoltaic hydrogen production

1. Introduction

Perovskite solar cells (PSCs) have made remarkable progress in recent years, with the efficiency of small-area cells now comparable to that of the state-of-the-art crystalline silicon solar cells. However, there is a theoretical upper bound for single-junction solar cells known as Shockley-Queisser (S-Q) limit. The S-Q limit is primarily determined by the semiconductor bandgap since only the above-bandgap photons can be harnessed for energy conversion while the below-bandgap photons are left unused. One way to break this limit is to go beyond the single-junction design and implement ways to harvest the full spectrum of solar photons from ultraviolet to infrared not barred by a single bandgap. Tandem solar cells (TSCs) [1–3], including Si/perovskite and perovskite/perovskite, are excellent examples for breaking the S-Q limit towards the fuller utilization of solar energy.

Carbon-based perovskite solar cells (C-PSCs) are low-cost type devices since the top electrode is made from carbon by a simple printing process. The carbon electrode is unique in that it can efficiently convert the full spectrum of solar photons to thermal energy. This motivates the concept of using C-PSCs for sequential conversion of the full-spectrum solar energy in a way analogous to TSCs. Specifically, C-PSCs can be conceptualized as an internally integrated system that combines a top PSC as the above-bandgap photon harvester with a bottom carbon-based heat converter and collector (C-HCC) as the below-bandgap photon harvester to jointly drive a water splitting electrolyzer, thereby circumventing the single junction S-Q limit in this particular sense. Notably, the C-HCC typically consists of graphite, carbon black, carbon nanotubes, or graphene, which not only has a solar absorption efficiency exceeding 90% across the entire solar spectrum but also undergoes rapid thermalization following the photoabsorption [4–7]. It is the synergistic harvesting of both the electrical energy generated by the PSC and the thermal energy by the C-HCC, that graded utilization of the full solar spectrum can be achieved with this dual-functional system. Plausibly, the theoretical efficiency limit achievable through such a combined electrical and thermal energy harvesting approach is expected to surpass the well-established S-Q limit of the single-junction photovoltaic devices [2,8,9].

To implement the C-PSC-based photothermal electrolyzer, it is important to understand the thermal response properties of the C-PSCs. In general, the operational temperature of photovoltaic (PV) cells is influenced by the ambient temperature and the incident irradiance intensity. Under conditions of high solar irradiance, thermal accumulation can lead to a substantial decline in power conversion efficiency (PCE), thereby significantly reducing the amount of electricity generated, particularly in conventional silicon-based solar cells. To counteract this performance degradation, photovoltaic power stations commonly employ supplementary cooling mechanisms such as air or water cooling to improve heat dissipation. However, these measures themselves introduce additional energy losses [8]. PSCs, especially the C-PSCs, are known to behave differently to our advantage in this aspect. We conducted a comparative analysis of the thermal behavior and overall performance between C-PSCs and conventional silicon cells under varying irradiance spectra and intensities. C-PSCs demonstrate distinct advantages in heat collection efficiency, bandgap tunability, and temperature-dependent performance characteristics, which make them particularly promising for application as top cells in graded solar energy utilization systems. By performing simulations based on the single junction S-Q framework, we determined the optimal bandgaps and the corresponding theoretical PV efficiency limits under different spectral and irradiance conditions. By integrating the experimental data with these simulated performance bounds, we systematically evaluated and validated the potential of perovskite solar cells to enhance graded utilization of the full solar spectrum.

Finally, to achieve an efficient and full-spectrum utilization of solar energy, this work thermally couple C-PSCs with an electrolytic water splitting (WS) cell to form a hybrid C-PSCs/WS system for hydrogen production. This integration enables the simultaneous harvesting of the above-bandgap photon for electrical energy and the below-band-gap photons for thermal energy, both of which are used to drive the WS electrolyzer, thereby significantly enhancing the overall energy efficiency in a graded solar energy utilization. Through strategic thermal management, not only are the detrimental effects of elevated temperatures on the performance of perovskite solar cells effectively mitigated, but the overpotential required for water electrolysis is also significantly reduced.

2. Results and Discussion

2.1. Photovoltaic and Photothermal Energy Conversion under Different Illumination Conditions

Figure 1a presents the outdoor solar spectra measured on a sunny day in Shenzhen, Guangdong, on 8 November 2024, at different times of the day. It clearly illustrates how the sun's low-angle trajectory through a thicker atmospheric layer during early morning and late afternoon results in enhanced attenuation of solar irradiance and a more pronounced variation in spectral composition. Within the atmosphere, the shorter-wavelength photons—such as those in the blue and violet regions—are preferentially scattered by Rayleigh scattering compared to the longer wavelength ones, such as those in the red and orange regions. This leads to an increased

proportion of long-wavelength light in the morning and evening spectra, which corresponds to a lower color temperature and an overall warmer appearance. In contrast, under overcast conditions, the absence of direct solar irradiance results in significantly reduced ground-level illumination. As depicted in Figure 1b, the resulting spectral distribution is dominated by high-color-temperature radiation, primarily due to the scattering of short-wavelength photons, which is characteristic of the diffuse light observed during cloudy days. This spectral shift imparts a cooler, bluer hue to the daylight. Given the continuous variation in solar spectra throughout the day and under different atmospheric conditions, graded energy harvesting strategies are essential for maximizing solar energy utilization. For example, multi-junction solar cells with tailored bandgaps offer a marked advantage over the conventional single-junction photovoltaic cells by harvesting the solar photons in a broader spectral range, and are critical for optimizing the performance of next-generation photovoltaic systems under real-world irradiance conditions [1,2]. Alternatively, as innovatively proposed in this work, single-junction solar cells based on the C-PSCs architecture can also enable the hierarchical utilization of solar energy by capturing below-bandgap photons that pass through the solar cell and converting them into thermal energy. This thermal energy, in conjunction with the nascent electrical power generated by the single-junction C-PSC, is then used to drive water electrolysis, thereby providing a unique way to go beyond the S-Q limit through hybrid photovoltaic–photothermal conversion.
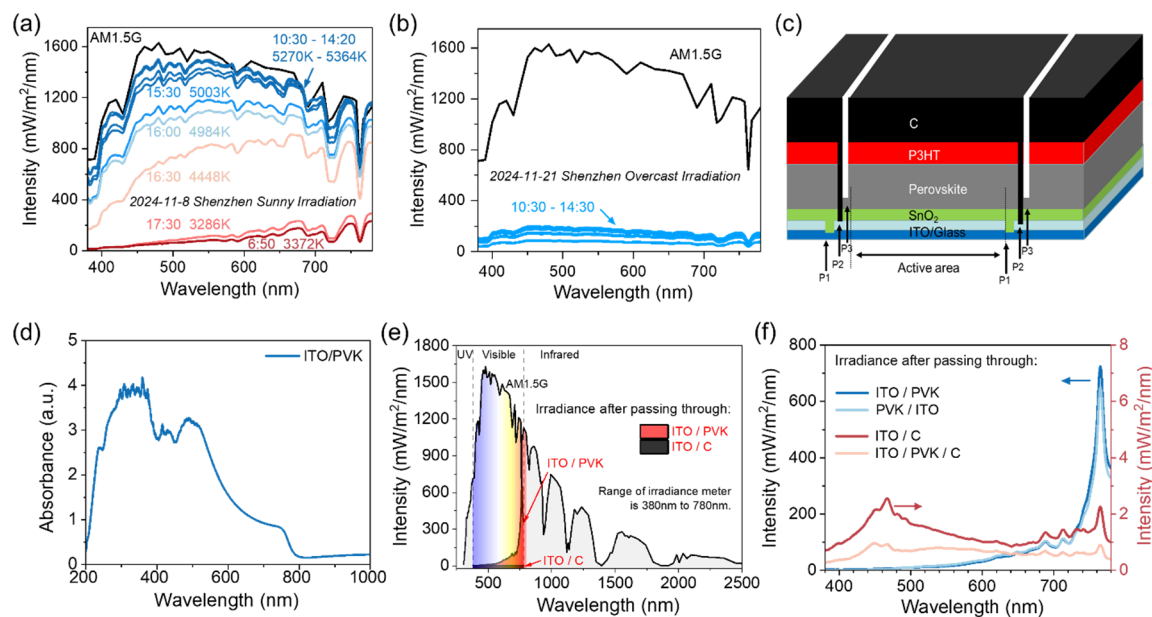

Figure 1. Spectral responses of C-PSCs to sunlight under various conditions. (**a**) Solar spectral variation on a clear day (8 November 2024), and (**b**) on an overcast day (21 November 2024), measured in Shenzhen, Guangdong. (**c**) Schematic diagram of the carbon-based perovskite solar modules (PSMs) structure, where the carbon electrode serves as the back electrode for C-PSMs as well as a Heat Absorber for Solar Grade Utilization System. (**d**) Ultraviolet-Visible (UV-vis) absorption spectrum of C-PSCs. (**e**) The spectral distribution of the AM1.5G simulated sunlight and the spectra after passing through different layers of C-PSCs in range spanning the UV-visible-infrared regions. (**f**) The spectral distributions of the AM1.5G simulated sunlight after passing through different layers of C-PSCs in the visible range.

Figure 1c schematically illustrates the architecture of the fully printed C-PSCs, which functions as both a photovoltaic cell and a heat absorber [10]. Consequently, this integrated configuration enables the stepwise and graded utilization of the full solar spectrum. As shown in Figure 1d, the UV–vis absorption edge of the perovskite film in our C-PSCs occurs near 800 nm, corresponding to an optical bandgap of approximately 1.55 eV. This is notably larger than the 1.12 eV bandgap of conventional silicon solar cells, making it particularly well-suited for use as a top cell in graded solar energy utilization systems. Indeed, the performance statistics presented in Figure 1e demonstrate that the wider bandgap of the perovskite film enables more efficient harvesting of short-wavelength photons under AM1.5G illumination by minimizing thermalization losses and enhancing the open-circuit voltage [1–3,11]. Furthermore, the spectral distribution of irradiance after passing through the specific multilayer structure is presented in Figure 1f. Notably, even after traversing a 500 nm-thick perovskite film, the long-wavelength irradiance around 765 nm remains as high as approximately 700 mW/m²/nm. This observation, combined with the UV-vis absorption spectrum of the perovskite material shown in Figure 1d and the corresponding AM1.5G spectral

irradiance profile depicted in Figure 1e, highlights the significant limitations inherent to single-junction photovoltaic devices in non-saturating the absorption of the effective spectral range and completely transmitting the ineffective spectral regions. Such inefficiencies lead to transmission losses unless the unused portion of the spectrum is harnessed through complementary design strategies. In conventional metal-electrode PSCs, this portion of the solar spectrum is typically reflected back into the atmosphere without being harnessed. In contrast, the C-PSC structure enables complementary and efficient harvesting of the untapped segment of solar spectrum by the carbon electrode, thereby enabling the effective capture and utilization of otherwise wasted photonic energy for thermal applications.

Although silicon cells are capable of exploiting a portion of the near-infrared spectrum (780–1127 nm), their narrower bandgap leads to more pronounced thermalization losses, thereby limiting the overall efficiency in converting high-energy photons into electrical energy. In contrast, the wider-bandgap perovskite layer in C-PSCs is capable of more effectively utilizing high-energy photons by minimizing thermal relaxation losses. Additionally, the carbon electrode efficiently harvests low-energy photons that lie beyond the absorption edge of the perovskite for photothermal conversion. As illustrated in Figure 1f, the ITO/C and ITO/PVK/C layers reduce the AM1.5G simulated irradiance to approximately 2.2 and 0.9 mW/m^2/nm at 765 nm, respectively. This design effectively mimics a tandem structure but operates within a broader framework aimed at overcoming the S-Q limit and achieving more comprehensive solar energy utilization [1,2,4]. Furthermore, according to literature statistics, perovskite solar cells exhibit significantly lower temperature coefficients compared to silicon cells [12–14], meaning that the increase in operating temperature results in a much smaller reduction in overall efficiency for perovskite cells. This feature underscores the advantage of C-PSCs in maintaining performance stability under fluctuating thermal conditions, further enhancing their suitability for integrated energy systems.

The adaptability of C-PSCs under varying spectral distributions, irradiance intensities, and temperature conditions represents a crucial research frontier in the development of hierarchical solar energy utilization systems tailored to the dynamic nature of real-world sunlight. Therefore, we conducted controlled indoor experiments using an AM1.5G Xenon Lamp solar simulator (Figure 2a) and a 3200 K white light-emitting diode (LED) source (Figure 2b), enabling a systematic investigation of the impact of different spectral compositions and irradiance levels on both heat collection efficiency and photovoltaic performance.
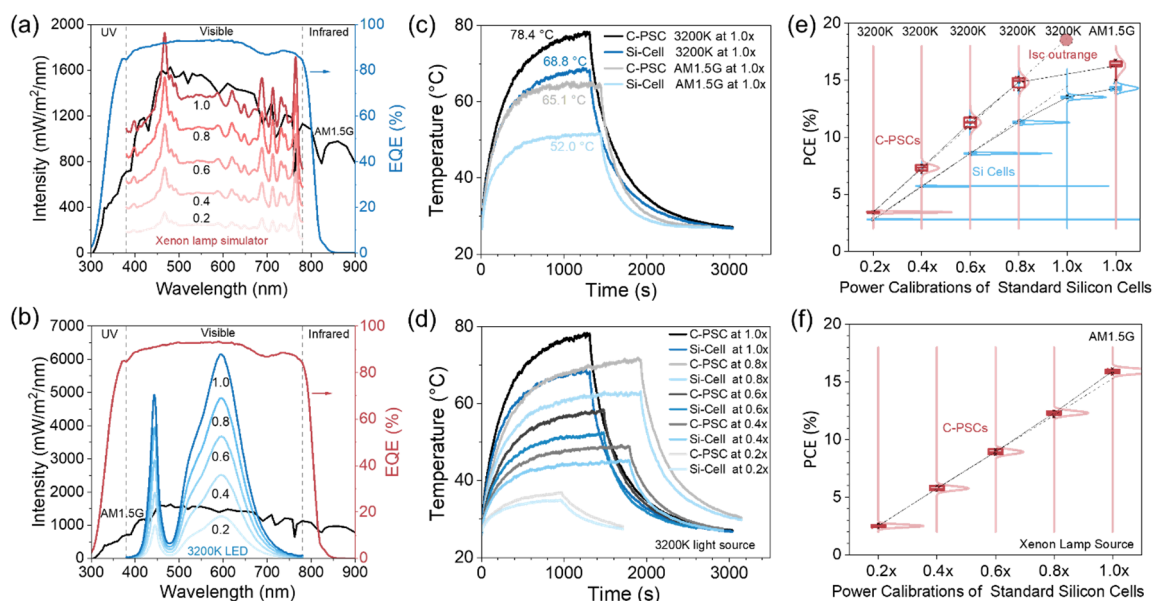

Figure 2. Photothermal conversion properties of C-PSCs under different illumination conditions. The intensity and spectral distribution of (**a**) xenon lamp solar simulator with AM1.5G filter (300–1200 nm) and (**b**) 3200 K LED light source spectrum under different power corrections for standard silicon cells. (**c**) Time dependent temperature variations of C-PSCs and silicon cells under irradiation of the 3200 K LED light source and the xenon lamp AM1.5G simulated light source calibrated by Newport standard silicon cells with its power of 1.0 time (the same calibration method used in the subsequent measurements). (**d**) Time dependent temperature variations of C-PSCs and silicon cells under irradiation of the 3200 K LED light source at irradiance levels of 0.2, 0.6, 0.8, and 1.0 times the full intensity. (**e**–**f**) The relationship between the power conversion efficiency and light intensity of C-PSCs under different irradiance intensities using (**e**) the 3200 K light source (with reference to silicon cells to reveal the effects of the all above bandgap photons) and (**f**) the AM1.5G simulator light source.

The irradiance intensities of both light sources were calibrated at room temperature using Newport's calibration system, based on the standard power output of a silicon reference cell under AM1.5G illumination conditions. The intensities were set to 1.0, 0.8, 0.6, 0.4, and 0.2 times the nominal value (Figure 2a,b). The spectral characteristics of both light sources at these irradiance levels were measured using a visible-range irradiance meter (380–780 nm) and are presented in Figure 2a,b. A critical observation from the external quantum efficiency (EQE) spectra presented in Figure 2a,b is that the infrared portion of the AM1.5G simulated sunlight falls outside the detectable range of the C-PSCs and thus cannot be converted into electrical energy. In contrast, the entire spectral distribution of the 3200 K light source lies within the EQE response band of the C-PSCs, thereby enabling efficient photon absorption across its emission spectrum. This distinction highlights the importance of spectral matching in optimizing photovoltaic performance and underscores the versatility of C-PSCs in capturing a broad range of solar wavelengths.

We then carried out temperature and performance measurements on both C-PSCs and silicon cells under these two light sources with illumination-on and illumination-off conditions, as part of a comparative study. As illustrated in Figure 2c, although the spectral range of the AM1.5G filter (300–1200 nm) broadly overlaps with that of silicon cells (300 nm–1127 nm), meaning that the majority of photons from the AM1.5G light source and all photons from the 3200 K light source are theoretically absorbable by silicon. However, the temperature rise curve observed in the silicon cell under 3200 K illumination reaches 68.8 °C and exhibits a steeper temperature increase trend, which is significantly greater than that observed under AM1.5G irradiance—only 52.0 °C with a more gradual progression. This observation underscores the critical role of spectral matching in determining both the photovoltaic and photothermal performance of solar cells under varying lighting conditions. Under the assumption that both light sources exhibit comparable reflectivity on the silicon cell surface, it becomes evident that the 3200 K light source, characterized by its shorter-wavelength, high-energy spectral distribution, induces substantial thermalization losses in narrow-bandgap silicon cells. As a result, the irradiance of the 3200 K light source—calibrated by the standard silicon cell at room temperature—exhibits a higher irradiance relative to that of the AM1.5G spectrum.

However, for wider-bandgap C-PSCs (black or grey curves), as shown in Figure 2c,d, these devices exhibit significantly higher operating temperatures than silicon cells under 3200 K illumination (~10 °C rise) and AM1.5G irradiation (~13 °C rise). These results highlight the exceptional optical absorption properties of carbon electrodes across diverse spectral ranges, as well as their enhanced thermal conversion efficiency. When accounting for the absence of surface reflection differences between the two cell types, the notably higher temperature observed in C-PSCs under 3200 K illumination can, at least partially, be attributed to the higher irradiance of the 3200 K light source, which was calibrated based on the power output of a standard silicon cell. Moreover, the wide-bandgap perovskite layer in C-PSCs experience reduced thermalization losses for the absorbed photons on the one hand, and leave a greater fraction of the incident below-bandgap photons to pass through the perovskite layer unabsorbed and reach the carbon electrode for efficient absorption and heat conversion on the other hand. As such, the unique value of C-PSCs is reflected not only by their capacity for effective optical harvesting but also by their efficient conversion of the below-bandgap photons to thermal energy, creating an integrated platform for photothermally enhanced electrolyzers that can mitigate the energy loss issues inherent in the conventional silicon-based PV systems [2].

Figure 2d presents the temperature rise curves of both C-PSCs and silicon cells under varying light intensities of the 3200 K light source, ranging from 0.2 to 1.0 times the calibrated standard power. As the irradiance level increases, the rate of temperature elevation in C-PSCs becomes markedly greater than that observed in silicon cells, with the temperature differential between the two systems growing more pronouncedly at higher intensities. Notably, while the photon energies of the 3200 K light source exceed the bandgaps of both C-PSCs and silicon cells—albeit to different extents—the resulting thermal behavior diverges significantly. Given that conventional silicon wafers possess a thickness on the order of hundreds of micrometers, the long wavelength above-bandgap photons are largely absorbed within the surface layer and cannot effectively penetrate through the cell structure. However, under the nearly identical illumination conditions, and assuming negligible differences in surface reflectivity, these photons together with the even longer wavelength photons generate a disproportionately higher temperature rise in C-PSCs, highlighting their superior capability for thermal energy conversion and collection.

This much higher thermal response of C-PSCs than silicon cells clearly arises from the more effective utilization of the below-bandgap solar photons by photothermal conversion through the carbon electrode. In silicon cells, the below-bandgap photons as well as the thermalization loss of the above-bandgap photons are dissipated as heat and subsequently lost to the surrounding environment. By contrast, the carbon electrode in C-PSCs is strategically positioned to efficiently thermalize the below-bandgap photons and capture the thermalization loss of the above-bandgap photons. As a result, the thermal conversion capability of C-PSCs not only surpasses that of

silicon cells but also increases with increasing light intensity, demonstrating their potential as an integrated platform for dual-mode photothermoelectric energy harvesting.

To effectively harness the significant temperature increase observed over irradiation time in Figure 2c,d, it is essential to assess device performance under prolonged irradiation conditions that encompass both operational states of the solar cells and scenarios involving solar-electric and solar-thermal cascade utilization, where thermal accumulation occurs. Figures 2e,f and S1–S3 present the photovoltaic performance of C-PSCs and silicon cells under various spectral conditions and light intensities, as determined by heat collection protocols involving 15 min of room-temperature illumination. As shown in Figure 2e, the dashed line represents extrapolated PCE values at 0.2–0.4× standard intensity, while the solid line shows averaged PCEs at adjacent levels. Silicon cells exhibit a slower PCE increase with rising light intensity, particularly between 0.8–1.0×, where the rise is much less pronounced than predicted. This trend aligns with data in Figure S1 in Supplementary Materials 1, which shows a decline in fill factor (FF) with increasing intensity, limiting PCE improvement. In contrast, C-PSCs display a significantly higher PCE growth rate, accompanied by a marked increase in short-circuit current, reflecting superior optical absorption and carrier generation efficiency. The superior performance of C-PSCs stems from their wider bandgap compared to silicon. Upon light absorption, electrons are excited and relax toward the conduction band minimum (CBM), with less energy lost due to the larger bandgap. This reduces thermalization losses, allowing more incident photon energy to be used for charge generation rather than heat dissipation, leading to higher PCE and greater efficiency enhancement under increased light intensity—highlighting a key advantage over silicon cells.

Figure 2e shows a higher efficiency of silicon cells under AM1.5G than under 3200 K light, due to temperature-induced degradation in silicon. PSCs, however, are less affected due to their lower temperature coefficient. Under the 1.0× 3200 K irradiation, The PCEs of C-PSCs exceeded the measurement range, but extrapolation from 0.2–0.8× data suggests higher PCE than AM1.5G. This is attributed to the shorter wavelength photons in 3200 K light, which reduce thermalization losses in wide-bandgap C-PSCs. Figures 2f and S3 show C-PSC performance under heat collection at increasing power levels (0.2–1.0×), using a 300–1200 nm xenon lamp with AM1.5G filter. At 65 °C, the PCE exceeded extrapolated values for lower intensities, consistent with the low temperature coefficient of C-PSCs.

2.2. Graded Utilization of Full Solar Spectrum by C-PSCs with the S-Q Framework as Benchmark

The S-Q limit [15] establishes a theoretical upper bound on the efficiency of a single p-n junction solar cell under ideal black-body radiation at a surface temperature of 6000 K based on the principle of detailed balance and the assumption that radiative recombination is the sole carrier loss mechanism within the solar cell. In this framework, bandgap is the main parameter intrinsic to a solar cell material. Only photons with photon energy $h_v \geq E_g$ are capable of generating electron-hole pairs through optical absorption, and this process occurs with 100% quantum efficiency. Conversely, photons with $h_v < E_g$ do not contribute to charge-carrier generation and are effectively "wasted" in conventional solar cells. This efficiency limit has become a benchmark for assessing the performance gap of an experimental solar cell. In this study, we adopt a distinctly different approach that leverages the dual functionality of C-PSCs to break the S-Q limit. This approach is illustrated in Figure 3a, which is essentially a dual-mode strategy with C-PSC and WS electrolyze connected in tandem. By effectively utilizing both the photon energy above (for PV conversion through the junction) and below (for photothermal conversion through the carbon electrode) the bandgap to drive the WS electrolyzer, C-PSCs represent a novel paradigm in solar energy harvesting that transcends the conventional limitations imposed by the single-junction photovoltaic systems.

To optimize the performance of the above-mentioned dual-mode photothermoelectrochemical devices based on C-PSCs and WS electrolyzers for graded solar energy utilization, accurate data on S-Q efficiency limits across varying temperatures and spectral distributions are essential. The bandgap energy of the perovskite plays a crucial role in determining its optical absorption and transmission characteristics, which in turn influences the PV efficiency of the junction and the photothermal conversion and collection efficiency of the carbon electrode of C-PSCs, and ultimately determines the efficiency of the WS electrolyzer driven jointly by the electrical and heat influxes therefrom. Apparently, the temperature of the C-PSCs arising from the photothermal conversion will become substantially higher than room temperature which is really we need to assist in the serially connected WS electrolyzer. Actually, in real-world outdoor conditions, the operating temperature of solar cells generally fluctuates dynamically [16], and during periods of intense solar irradiance, temperatures can rise significantly above 300 K. However, the conventional S-Q limit is typically evaluated at a standard cell temperature of 300 K.

To fill this gap and systematically explore the energy conversion characteristics of the dual-mode device, we conducted extensive simulation calculations of S-Q efficiency limits under different operational conditions,

including temperature variations, spectral distributions, and bandgap values. The results from these simulations are compiled in Supplementary Materials 2 (Excel Tables), where we integrated both the standard AM1.5G spectrum and measured solar spectra obtained in Changshu on 6 September 2024, and 21 November 2024.
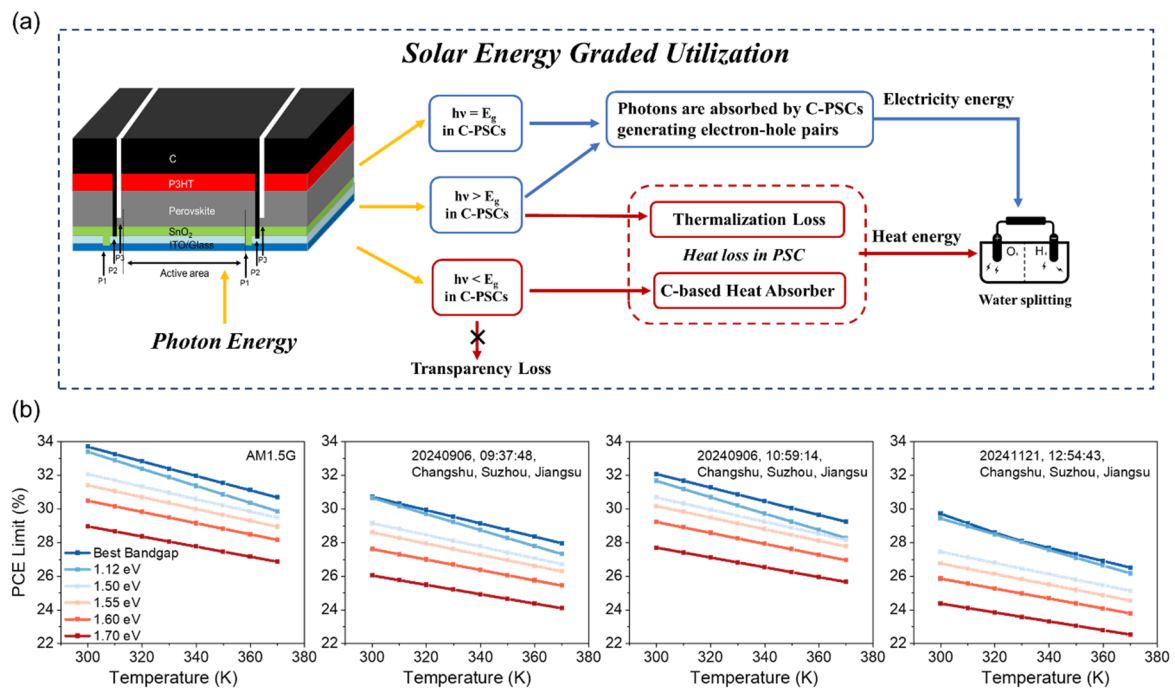

Figure 3. Graded solar energy utilization of C-PSCs guided by the S-Q framework. (**a**) Schematic diagram to conceptualize the graded utilization of full spectrum solar energy into electrical energy and thermal energy in pursuit to break the S-Q efficiency limit. (**b**) The line plots of PCE limits as a function of temperature for different bandgap solar cells and under various actual solar spectra based on the simulation calculations for the S-Q efficiency limit (detailed performance data are listed in the Supplementary Materials 2).

This comprehensive dataset enables us to determine key photovoltaic parameters—such as optimal bandgap, open-circuit voltage (Voc), short-circuit current (Isc), fill factor (FF), and power conversion efficiency (PCE) limits—for solar cells operating at various temperatures. The PCE limit data from the simulation are presented in Figure 3b and S4, where they are used to analyze how PCE limits vary with temperature for materials with different bandgaps.

As illustrated in Figure 3b, the calculated PCE limits exhibit a strong dependence on both the solar spectrum and operating temperature. The blue lines in these figures (labeled as "best bandgap") represent the maximum achievable PCE at the optimal bandgap for each respective temperature. When compared to other curves corresponding to fixed bandgap values, it is evident that PCE decreases with increasing cell temperature regardless of the bandgap.

To enhance the efficiency of single-junction solar cells, reducing the operating temperature is an important strategy. However, in the context of photothermoelectric system for graded utilization of full solar spectrum, we find that an alternative approach could offer even greater potential for performance enhancement. Specifically, by judiciously controlling both the system's temperature and the bandgap of the top cell, it becomes possible to combine the conventional PCE limit with an additional photothermal energy conversion efficiency component. This integrated strategy allows the overall efficiency limit of such systems to surpass that of traditional single-junction solar cells, demonstrating a promising pathway toward more efficient and multifunctional photovoltaic–photothermoelectric hybrid devices.

As illustrated in Figure 3b and S4, the line plots corresponding to a bandgap of 1.12 eV represent the relationship between power conversion efficiency (PCE) limits and temperature for silicon solar cells, whereas the curves for 1.5, 1.55, 1.6, and 1.7 eV correspond to conventional perovskite materials with varying bandgaps. As temperature increases, the slopes of the PCE limit versus temperature curves for these perovskite materials are shallower compared to that of silicon. This indicates that the performance degradation of perovskite-based systems under elevated temperatures is less pronounced, making them more robust in maintaining both electrical and thermal energy conversion efficiency.

This reduced sensitivity to temperature rise suggests that perovskite materials are particularly well-suited for photothermoelectric conversion in a graded utilization of full solar spectrum configurations, which can ensure stable performance across a range of operating conditions that integrate heat and electricity collection for water splitting. Consequently, their inherent lower temperature coefficients make them superior candidates for achieving high-efficiency dual-mode solar energy conversion systems, capable of maintaining high PCE limits even when subjected to thermal fluctuations.

Through the novel tandem structure we propose, the C-PSC enables the graded utilization of full-spectrum solar energy by harvesting high-energy photons within the wide-bandgap perovskite layer for electricity generation, while low-energy photons are absorbed and converted into thermal energy via the carbon electrode. To further enhance the utility of the collected thermal energy, we have designed a demonstration device (as shown in Figure 3a), which integrates PV and thermal coupling for water splitting-based hydrogen production through the C-PSC/WS system.

This integrated approach not only mitigates losses associated with rectification and power transmission in conventional PV systems but also enables on-site direct current (DC) utilization for electrolytic water splitting, thereby improving overall energy efficiency. The output from the photovoltaic component exhibits significant variability between day and night, with an inherently unstable generation profile. By leveraging the C-PSCs to produce hydrogen through electrolysis, this intermittent electrical power can be converted into a storable chemical fuel—hydrogen—which helps to smooth out the power generation curve over time.

Furthermore, the surplus electricity generated by the PV system during periods of high irradiance can be fed into the grid for later use. Meanwhile, hydrogen production via water splitting is particularly advantageous when electricity demand is low and prices are reduced, leading to a significant decrease in the cost of hydrogen generation. This strategy not only enhances the economic viability of solar energy utilization but also enables long-term energy storage and flexible distribution of clean hydrogen as an alternative fuel source. Thus, the C-PSC/WS system represents a promising pathway toward sustainable and efficient solar-to-hydrogen conversion under real-world operating conditions.

2.3. Integration of C-PSC and WS Electrolyzer for Photothermoelectrochemical Energy Conversion

In principle, the utilization of waste heat from solar cells to promote water splitting not only mitigates the adverse effects of elevated temperatures on perovskite solar cells but also significantly reduces the overpotential required for electrolytic water splitting, thereby enhancing overall system efficiency. In this work, a dedicated thermal management system is employed to capture and transfer the heat loss generated by the C-PSC to the WS electrolyzer. Figure 4a outlines the operational principle and system architecture of the thermal management setup. The system employs a circulating coolant to remove waste heat from the solar cells and channel it to the electrolytic cell, thereby enhancing electrolytic efficiency through thermal integration. A copper cooling head facilitates efficient heat absorption from the solar cells, transferring it to the coolant and maintaining optimal operating temperatures. A peristaltic pump ensures continuous circulation of the heated coolant between the cooling head and the electrolytic cell, enabling effective thermal exchange. To further enhance heat transfer, silicone grease is applied at the interface between the solar cell and the cooling head, improving thermal conductivity and system performance.

Given the high operating voltages of large-area solar cells, multiple electrolytic units are connected in series to align with the maximum power point (MPP) of the photovoltaic system, thereby minimizing the coupling losses. To construct a multi-cell electrochemical device, individual electrolytic cells are isolated by insulating barrier bags and enclosed within a chamber fabricated from polytetrafluoroethylene (PTFE), as illustrated in Figure S5. The electrochemical cells employ platinum/carbon (Pt/C) as the cathode catalyst and ruthenium dioxide (RuO_2) as the anode catalyst. To monitor thermal dynamics across the system, thermocouples are strategically positioned on the surface of the solar cell, within the electrolytic chamber, and in the ambient environment, as depicted in Figure S6. Furthermore, a thermal imaging camera is employed to visualize spatial temperature distributions, revealing that both perovskite solar cells (PSCs) and the electrolysis units operate at temperatures significantly above ambient conditions, as shown in Figure 4a.

Figure 4b shows that over a continuous operational period of 2500 s, the temperature of the electrolyte fluctuated within a narrow range of 34 °C to 34.5 °C, while the solar cell surface temperature ranged between 36 °C and 36.5 °C. The small fluctuations in electrolyte temperature may be attributed to minor variations in the peristaltic pump's flow rate. Similarly, the temperature of the solar cell was also subject to slight variations due to the thermocouple's surface placement and potential environmental interference from air currents. Despite these minor fluctuations, the thermal management system successfully maintained an average electrolysis cell temperature of 34 °C, a substantial increase over the ambient temperature of 22.5 °C. A quantitative analysis of

the heat transfer process demonstrates that the system achieves a remarkable heat collection efficiency of 74.4% and exhibits excellent thermal conductivity performance (Figure S7).
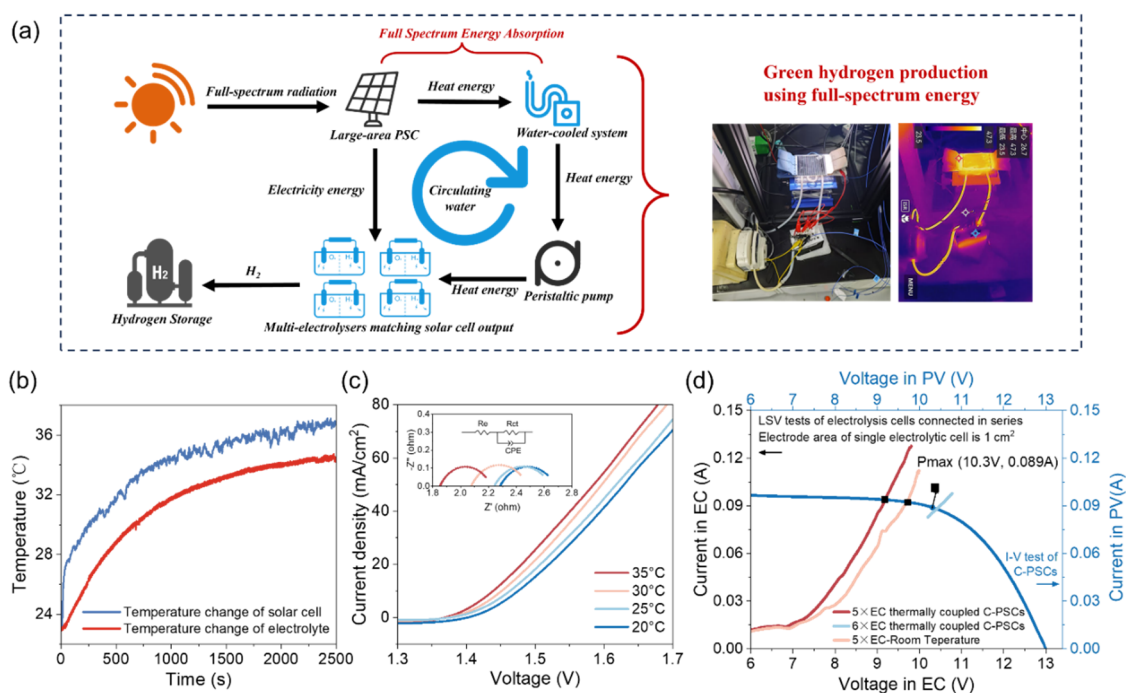

Figure 4. Integration of C-PSC and water-splitting electrolyzer for photothermoelectrochemical energy conversion. (**a**) Schematic diagram of heat management system and structure of the photo-thermo-electrochemical energy conversion system. (**b**) Variations of electrolyte temperature with time for solar cell and electrolyzer. (**c**) LSV curves and EIS (inset) of the Pt/C//RuO$_2$ for a single electrolytic cell at different temperatures (electrode area is 1 cm^2). (**d**) I–V curve of C-PSC (the dark blue line) and two-electrode operating I–V characteristics of 5 and 6 series-connected electrolysis cells (with and without the photothermal coupling) in water electrolysis.

This efficient thermal management not only enhances the stability and longevity of perovskite solar cells under elevated temperatures but also significantly improves the thermodynamic driving force for water splitting, thereby promoting solar-to-hydrogen conversion. The results confirm that this integrated system offers a viable pathway toward sustainable and high-efficiency photothermoelectric hydrogen production. The rise in temperature plays a crucial role in diminishing the overpotential required for water electrolysis and improves the hydrogen production efficiency. Figure 4c presents the linear sweep voltammetry (LSV) curves of Pt/C//RuO$_2$ electrodes at various temperatures, demonstrating a clear trend: as the temperature increases, the overpotential for water splitting decreases progressively. This reduction in overpotential can be attributed to several interrelated factors. First, elevated temperatures provide increased thermal energy to the reactant molecules, thereby enhancing their kinetic energy. This leads to more effective breaking of chemical bonds during the water-splitting reaction and lowers the activation energy barrier that must be overcome for the process to occur. As a result, less overpotential is required to drive the electrolysis under these conditions. Moreover, higher temperatures enhance the ionic mobility within the electrolyte, increasing its conductivity and reducing ohmic resistance. This effect is further supported by the electrochemical impedance spectroscopy (EIS) results shown in Figure 4c, which reveal a progressive decrease in solution resistance as temperature increases. Lower internal resistance translates to improved charge transfer efficiency, thereby contributing to the observed reduction in overpotential during electrolysis. These findings underscore the beneficial role of thermal management in enhancing the electrochemical performance of water-splitting systems and highlight the synergy between photothermal energy harvesting and efficient hydrogen production.

Since the maximum output voltage of the solar cell is 10.3 V, five electrolytic cells are connected in series to match this voltage and minimize coupling losses between the PV system and the electrolysis unit. At room temperature, the system operates at an electrolysis current of 92.1 mA and a working voltage of 9.78 V. Using the formula for solar-to-hydrogen efficiency:

$$\eta_{STH} = \frac{1.23 \times I_{op} \times N \times FE}{P_{Sun}}$$

in which, I_{op} is the operating current, N is the number of electrolytic cells, and P_{Sun} is the incident solar power [17]; with FE representing the Faraday efficiency. Faraday efficiency tests were conducted on the cathode catalyst by drainage method (Figure S8a). The average Faraday efficiency from six independent measurements was 99.73% (Figure S8b,c). As a result, we obtained an overall system efficiency of 11.30% without thermal management, which can be seen in Figure 4d (the orange curve).

Now when the electrolyte was subjected to thermal management, its temperature increase promotes electrolytic current to 94.1 mA at an operating voltage of 9.07 V, as can be seen in Figure 4d (the red curve). This current increase led to an elevation in the solar-to-hydrogen (STH) efficiency to 11.54%, yet the working voltage fell further below the maximum power point (MPP) of the solar cell, leaving even more room for reclaiming the residual coupling losses. For further efficiency improvement, an extra electrolytic unit was integrated into the hydrogen production system to better align with the MPP of the photovoltaic device and minimize energy loss during power transfer. On the basis of the MPP data from the series-connected module, we calculated the optimal driving power for the electrolytic cells as illustrated in Figure 4d. Due to the reduced overpotential for water splitting at elevated temperatures and the subsequent increase in current density, the system was able to accommodate an additional load. By incorporating the sixth electrolytic cell into the series connection, it became possible to raise the operating voltage closer to the MPP of the solar cell, thereby reducing coupling losses and enhancing energy conversion efficiency. Then came a technical issue due to the limited measurement range of the electrochemical workstation (−10 V to +10 V), so it was not feasible to measure the output parameters for six electrolytic cells in series. Therefore, a direct current (DC) power supply and multimeter were employed to determine the coupling voltage and current of the solar cell–electrolyzer system. As shown in Figure 4d (the short light blue line crossing the photovoltaic I–V curve), by aligning these measured values with the I–V characteristics of the solar cell, an operating current of 88.2 mA was recorded, finally yielding an STH efficiency of 12.98%. Since the original and thermally coupled systems exhibited STH efficiencies of 11.30% and 12.98%, respectively, the thermal management has significantly boosted the STH efficiency by 14.86%, demonstrating the high potential for utilizing the waste heat to enhance water-splitting performance and the overall system efficiency.

Moreover, to evaluate the long-term stability and reliability of the system under the thermal management condition, we conducted prolonged operation tests and monitored changes in both STH efficiency and temperature over time. As shown in Figure S9, the operating temperature change of both solar cell and electrolyte remained stable after operating for 35 min. Furthermore, as illustrated in Figure S9a, when the electrolyte was circulated solely by the peristaltic pump with the thermal management system deactivated (i.e., the cooler disconnected from the solar cell), the electrolyte temperature remained stable over time, showing no significant increase. This finding clearly demonstrates that the heat generated by the operation of the peristaltic pump has a negligible impact on the elevation of the electrolyte temperature. Therefore, the temperature rise observed in the fully operational system can be primarily ascribed to heat transfer from the solar cell rather than to the circulation pump. Figure S10 presents a comparative analysis of STH efficiency with and without thermal management: the heat unregulated system had an initial efficiency of 10.5% with minimal gain over time, whereas the heat managed system showed a stable and substantial increase, climbing to 11.7% after 35 min. Furthermore, both the catalyst employed in this system and the solar cells demonstrate excellent stability under the same operating conditions as the coupled system, fully demonstrating the system's potential for long-term stable operation. Figure S11 demonstrates that the Pt/c‖RuO$_2$ electrode maintains stability for over 200 h at a current density of 100 mA cm^{-2}, which closely approximates the operating current density of the coupled system. We further validated the long-term thermal stability of C-PSCs under high-temperature conditions. The Maximum Power Point Tracking (MPPT) test (Figure S12) provides direct evidence of the exceptional operational stability of C-PSCs under rigorous conditions—approximately 80 °C and less than 10% relative humidity—retaining over 95% of its initial performance after approximately 500 h of continuous operation. This test was specifically designed to evaluate stability under high-temperature stress, a condition known to accelerate degradation mechanisms such as ion migration and electrode corrosion. The results underscore the remarkable resilience of C-PSCs even in harsh thermal environments.

The stability advantage of carbon-electrode perovskite solar cells is more obvious when compared with the metal-electrode counterparts. As illustrated in Figure S13, metal electrodes exhibit significant reactivity with perovskite halides, leading to rapid degradation and the formation of yellow, non-photoactive phases—even under mild environmental conditions such as low temperature and mild humidity. In contrast, C-PSCs show no visible morphological or optical changes under identical testing conditions, maintaining outstanding stability over time with minimal efficiency loss.

It is noted that the high reflectivity of traditional metal back electrodes (e.g., Au, Ag) enhances the short-circuit current density (Jsc) and PCE of PSCs through the "photon recycling" effect, which extends the optical path within the perovskite layer. However, that optical path extension only applies to the wavelengths of incident

light that the perovskite can efficiently absorb, for example, in metal-electrode-based PSCs with film thicknesses typically below 350 nm [18,19]. Furthermore, the optical path extension to enhance Jsc and PCE has almost saturated for our 500 nm perovskite layer thickness in carbon-based PSCs (C-PSCs) (Figure S14). As shown in Figure 1e, the spectral distribution of transmitted irradiance through the ITO/perovskite layers (ITO/PVK, the red region) indicates that photon capture in the visible range is nearly saturated at this thickness. Thus, it is difficult to further improve Jsc and PCE by merely extending the optical path. More importantly, over 43% of the sunlight below the bandgap can not be absorbed by the perovskite materials for photovoltaic conversion [4], but can be converted to heat efficiently by the carbon electrode for assisting in water splitting in the series-connected electrolytic cell.

The carbon electrode, besides its high conductivity, not only exhibits favorable energy level alignment with the perovskite layer (work function ≈ 5.0 eV) for efficient charge extraction [20], but also serves as a highly effective photothermal conversion layer. As evidenced by the temperature rise profile in Figure S15, the carbon electrode plays a dominant role in the full solar spectral absorption in C-PSCs, outperforming its Cu-electrode counterpart. This is enabled by its intrinsic black color, which provides broadband absorption from UV to infrared, allowing it to utilize sub-bandgap photons inaccessible to metal electrodes. Furthermore, carbon materials exhibit high photothermal conversion efficiency (80–90%, surpassing the 40–70% of metal nanoparticles) [21] and superior in-plane thermal conductivity (up to 1500–2000 $W \cdot m^{-1} \cdot K^{-1}$ for graphite) [6,22,23]. This high thermal conductivity facilitates rapid and efficient dissipation of the generated heat to the electrolyte, thereby promoting the water-splitting reaction while minimizing overheating within C-PSCs. We also characterized the electrical properties of the carbon electrode. A sheet resistance measurement was performed on the carbon electrode using a four-point probe system (Jandel RM3000+), giving a value of 7.02 Ω/sq. Additional variable-temperature Hall measurements (CH-500 system) provided the following parameters: sheet resistance of 7.846 Ω/sq, electrical conductivity of 4.248×10^3 S/m, bulk carrier concentration of 3.169×10^{19} cm^{-3}, and carrier mobility of 8.380 cm^2/V·s. These results confirm that the carbon electrode combines relatively high electrical conductivity, comparable to graphite-based materials, with effective thermal management capability.

Next, different bandgaps of perovskite were investigated, which were acieved by varying the Br/I ratio. As shown in Figure S16a, the perovskite bandgap widens with an increasing Br/I ratio, the growing fraction of sub-bandgap photons results in a milder temperature rise in the standalone perovskite layer, indicating its enhanced optical transmission. In contrast, the complete C-PSC devices incorporating carbon electrodes (Figure S16b) maintain a consistent thermal response regardless of the bandgap variation. This key observation highlights the carbon electrode's ability to not only absorb and thermally convert both transmitted above-bandgap photons and sub-bandgap photons, but also capture and utilize the thermal energy released from non-radiative recombination from the perovskite layer.

In terms of photovoltaic performance change, as summarized in Figure S16c, a substantial increase in the Br/I ratio from 0 to 1/1 and the corresponding widening in bandgap led to a PCE decrease from 18.07% to 16.6%. While this variation in PCE is appreciable, its impact on the overall photothermal performance remains relatively minor in the context of full-spectrum solar energy utilization. This is because the temperature rise is primarily governed by the photothermal conversion of sub-bandgap photons—which account for nearly half of the solar spectrum—together with the thermal energy harvest out of non-radiative recombination arising from the above-bandgap photons. Furthermore, we conducted tests on a batch of C-PSCs and observed that the efficiency demonstrated a high degree of consistency (Figure S17).

While higher STH efficiencies have been reported in prior studies, those results were often achieved by relying on high-performance, non-commercial PV cells or costly multi-junction concentrator systems, such as double- or triple-junction devices. Secondly, the true merit of a solar-to-hydrogen system lies not solely in its absolute STH efficiency but the normalized STH/PCE ratio is also of great significance—a metric that reflects the conversion efficiency from electrical power to hydrogen production independent of the inherent PV efficiency. This ratio provides a more meaningful comparison across different systems, as it isolates the performance of the electrochemical water-splitting process from variations in PV cell quality. In this study, the solar-to-hydrogen system achieves an STH/PCE ratio of 71.0%, which surpasses most prior related studies reported in the literature (Table S1). This result highlights the effectiveness of the thermal management strategy in enhancing the overall efficiency of hydrogen production by leveraging waste heat from the solar cell to reduce the overpotential of water electrolysis. Furthermore, this work employs a large-area solar cell (50 cm^2) integrated with the hydrogen production unit as compared to the typically less than 1 cm^2 cells used in previous studies, demonstrating the feasibility of scaling up the technology for real-world deployment.

To sum up, the combination of an effective thermal management strategy and the use of a large-area solar cell represents a significant step forward in the development of efficient and scalable solar-to-hydrogen conversion

systems. This efficient thermal management not only enhances the stability and longevity of perovskite solar cells under elevated temperatures but also significantly improves the thermodynamic driving force for water splitting, thereby largely promoting solar-to-hydrogen conversion. The results confirm that this integrated system offers a viable pathway toward sustainable and high efficiency photothermoelectric hydrogen production.

3. Experimental Section

3.1. Materials and Reagents

All chemicals and solvents were commercially sourced and used as received without further purification. Methylammonium Hydrochloride (MACl) and Formamidinium Iodide (FAI) were purchased from Greatcell Solar Materials Co., Ltd. (Queanbeyan, Australia), while Lead Iodide (PbI_2) and Lead Bromide ($PbBr_2$) were obtained from Advanced Election Technology Co., Ltd. (Yingkou, China). The colloidal dispersion of SnO_2 nanoparticles (15% in H_2O) and Cesium Iodide (CsI) were purchased from Xi'an Yuri Solar Co., Ltd. (Xi'an, China). The anhydrous grade solvents, including Dimethyl Sulfoxide (DMSO), N,N-Dimethylformamide (DMF), 1,3-Dimethyl-3,4,5,6-tetrahydro-2(1H)-pyrimidinone (DMPU), were purchased from J & K Co., Ltd. (Xi'an, China). Conductive carbon slurry was acquired from Guangzhou Saidi Technology Development Co., Ltd. (Guangzhou, China), Potassium hydroxide (KOH) was purchased from Energy Chemical Co., Ltd. (Shanghai, China).

3.2. Preparation of Carbon-Based Perovskite Solar Modules (PSMs)

To fabricate the carbon-based PSMs, a 10 cm × 10 cm ITO glass substrate was first scribed with P1 laser etching and then cleaned by ultrasonic washing using detergent, deionized water, and ethanol for 10 min to ensure a clean and smooth surface. After the cleaning process, the substrate was dried in an oven at 70 °C and subjected to ultraviolet-ozone treatment for 30 min to enhance surface hydrophilicity. Next, the SnO_2 layer was deposited on the ITO substrate by slot die coating with the colloidal dispersion of SnO_2, which had been diluted fourfold with deionized water. The SnO_2-coated ITO was then annealed at 150 °C for 30 min to remove any residual solvent and obtain the SnO_2 film.

For the perovskite layer, a $FA_{0.85}Cs_{0.15}PbI_3$ precursor solution was prepared by dissolving PbI_2 at a concentration of 1 M in a ternary solvent mixture of DMF, DMSO, and DMPU, with a volume ratio of 0.85:0.1:0.05. To suppress the formation of δ-$FAPbI_3$, a 15% molar ratio of MACl relative to FAI and a 2.5% mass ratio of $PbBr_2$ relative to PbI_2 was added to $FA_{0.85}Cs_{0.15}PbI_3$ precursor solution to fabricate the perovskite precursor solution of $FA_{0.85}Cs_{0.15}PbI_{(3-x)}Br_x$. The precursor solution was then printed on the SnO_2-coated substrate using the slot-die coating, followed by annealing at 150 °C for 30 min to facilitate perovskite crystallization.

After the perovskite layer was formed, the film was conducted P2 and P2.5 laser etching. The film was then coated with carbon slurry through screen printing. The carbon-based PSMs consist of 12 sub-cells were completed and the active area of PSMs was designed as 50 cm^2 after the P3 laser etching and P4 laser edge cleaning.

3.3. Characterization and Device Performance

The sunlight spectra and light source spectra were measured using a spectral color illuminance meter (HP330P, 380–780 nm, DUOTONE CLOUD Co., Ltd., Hangzhou, China). Temperature recordings for solar cells and electrolytic cells were captured by a multi-channel temperature recorder equipped with a K-type thermocouple probe, with a test interval set to 0.1 s (TCP-8, MEASUREFINE Co., Ltd., Zhongshan, China). Thermal imaging photos were recorded using the infrared thermal Imager (HM-TPK20-3AQF/W, HIKMICRO Co., Ltd., Hangzhou, China). UV-vis absorption spectra were measured with a QE65Pro spectrometer (Ocean Optics). The temperature-time curves and current-voltage performance tests of the solar cells under narrow-wavelength spectra were conducted using a 3200 K color temperature white light LED source (GSYGY-00.01, GSOLAR POWER Co., Ltd., Xi'an, China) This LED emits light composed of approximately 36.8% red, 48.2% green, and 15% blue spectral components, and 15% blue components, excluding both ultraviolet and infrared radiation. The standard current-voltage curves of PSMs without antireflection coating were measured under a xenon lamp solar simulator (LSS-100, 3A Class Solar Simulator, LightSky Tech. Co., Ltd., Taiwan, China) with an AM1.5G optical filter (300–1200 nm). For both light sources, varying irradiance intensities were calibrated using a standard silicon cell measurement system (Newport, 91150V, 2424, USA). The heat collection temperature measurements were conducted under controlled environmental conditions of 30%RH to 80%RH and at room temperature in ambient air. The current-voltage scan was set as 0.1 V per 10 ms. The External Quantum Efficiencies (EQE) were determined using a detector responsivity measurement system calibrated with a standard silicon cell (SCS10-X150A-DSSC-CB07l, Zolix Co., Ltd., Guangzhou, China). The sheet resistance of the carbon electrode was

measured using a four-point probe system (Jandel RM3000+). The electrical properties of the carbon electrode were analyzed using the CH-500 variable-temperature Hall measurement system (CH-Magnetoelectricity Technology, Beijing, China).

Electrochemical measurements were performed in a PETT cube cell containing 1 M KOH electrolyte. Standard two-electrode and three-electrode systems were used, with a working electrode, a Hg/HgO reference electrode and a Pt coil counter electrode connected to a potentiostat (CHI760E). Electrochemical impedance spectroscopy (EIS) was carried out from 1 Hz to 100 kHz.

3.4. Details of Simulation Based on Shockley-Queisser Limit Theory

The Shockley-Queisser (S-Q) limit is presented under the detailed balance limit and ideal conditions. In S-Q limit, the current-voltage curve is calculated according to the formula

$$J(V_{\text{applied}}) = J_{\text{p}} - J_{\text{rad}}(V_{\text{applied}}) \tag{1}$$

Here, $J_{\text{p}} \cong q \int_{E_g}^{\infty} \frac{2\pi}{h^3 c^2} \frac{E^2}{exp\left(\frac{E}{k_{\text{B}}T_{\text{sun}}}\right)-1} dE$ and $J_{\text{rad}}(V_{\text{applied}}) \cong q \int_{E_g}^{\infty} \frac{2\pi}{h^3 c^2} \frac{E^2}{exp\left(E-\frac{qV_{\text{applied}}}{k_{\text{B}}T_{\text{cell}}}\right)-1} dE$ stands for

photocurrent density and radiative recombination current density, respectively. V_{applied}, q, E_{g}, h, c, k_{B}, T_{sun}, T_{cell} are the applied voltage, elementary charge, band gap, Planck's constant, speed of light, Boltzmann constant, temperature of sun and temperature of cell. The power conversion efficiency (PCE) is calculated according to the formula

$$\eta = \frac{\text{maximum}(J(V_{\text{applied}}) \times V_{\text{applied}})}{P_{\text{in}}} \tag{2}$$

where $P_{\text{in}} = \frac{2\pi}{h^3 c^2} \int_0^{\infty} \frac{E^3}{exp\left(\frac{E}{k_{\text{B}}T_{\text{sun}}}\right)-1} dE$ is the input illumination power density [15,24,25].

4. Conclusions

Surpassing the S-Q efficiency in a broad sense is the holy grail for the future development of green solar energy. Towards this end, the present study has demonstrated the potential of using the C-PSCs to break the S-Q efficiency limit and enable the graded utilization of solar energy into electrical energy and thermal energy. In the system for the proof of concept, photons with energy higher than the perovskite bandgap are converted into electrical energy by the perovskite layer, while photons not converted into electricity are transformed into thermal energy by the carbon electrode. Correlative studies are pioneered on the integral photothermoelectrical energy conversion under heat-accumulated conditions that link solar cell performance with the spectral distribution and intensity. Distinctive advantages of the C-PSCs are manifested in terms of power conversion efficiency, heat collection efficiency, temperature coefficients, and the overall utilization efficiency of full-spectrum solar energy.

In the graded sunlight utilization system, solar cells need to operate at relatively high temperatures, whereas the conventional S-Q efficiency limit is calculated for cells at 300 K. To address this, we developed a simulation model for the S-Q efficiency limit, enabling evaluation of the performance limits of solar cells under varying temperatures, spectral distributions and intensities of irradiation and materials with different bandgaps. This simulation model provides a roadmap for achieving the ultimate overall efficiency limits of both electrical and thermal energy in the graded sunlight utilization systems.

In exploring methods for utilizing electrical and thermal energy in the graded solar energy utilization systems, we propose a feasible demonstration device that couples C-PSCs with a water electrolysis cell to form a photothermoelectric hybrid system (C-PSCs/WS). In this configuration, the electrical energy generated by C-PSCs is used for hydrogen production via water electrolysis, while the thermal energy collected by the carbon electrode is used to heat up the electrolysis cell for boosting the hydrogen production. Through this photothermoelectric coupling, heat exchange occurs between the C-PSCs and the electrolyzer, and increasing the electrolyzer temperature considerably improves the catalytic activity of the water splitting reaction. Ultimately, this integral system enables efficient, localized graded utilization of solar energy through the C-PSCs based design. The solar-to-hydrogen efficiency (STH) increased from 11.30% to 12.98%, a rise of 14.86%, with an STH/PCE ratio as high as 71.0%. This work establishes that the photothermoelectric coupling system of C-PSCs/WS is a viable and highly promising model for the efficient graded utilization of solar energy.

Supplementary Materials

The additional data and information can be downloaded at: https://media.sciltp.com/articles/others/2603091 602130449/MM-25120044-Supplementary-Materials.zip. Supplementary Materials 1: Figure S1: Performance

statistics of C-PSCs and silicon cells under 3200 K light source with varying illumination intensities and under standard AM1.5G light source. Figure S2: Current-voltage scan curves of C-PSCs and silicon cells under 3200 K light source with varying illumination intensities and under standard AM1.5G light source. Figure S3: Performance statistics of C-PSCs under Xenon lamp source with AM1.5G filter with varying illumination intensities. Figure S4: The line plots of PCE limits and temperature for different bandgap materials using the actual outdoor sunlight spectrum (detailed performance data are listed in the Supplementary Materials 2). Figure S5: Schematic diagram of separating electrolytic cells using barrier bags. Figure S6: Graded solar energy utilization system for thermoelectric coupling water splitting demonstration. Figure S7: Variations of electrolyte temperature with time for solar cell and electrolyzer in the beginning 90 s. Figure S8: Faraday efficiency test (**a**) Faraday efficiency test set (**b**) Recording of volume of hydrogen production and corresponding time (**c**) Result of Faraday efficiency measurement six times (left), average faraday efficiency with error bar (right). Figure S9: Temperature change of Solar cell and electrolyte (**a**) without heat management system and (**b**) with heat management system. Figure S10: The solar cell module is cut into two series sub-cells to measure the change in STH of a single electrolytic cell over time. Figure S11: Stability of Pt/C‖RuO$_2$ at 100 mA cm^{-2} current density in two electrode system. Figure S12: Maximum Power Point Tracking (MPPT) test of unencapsulated carbon electrode-based perovskite modules. Figure S13: Photographs of (**a**) carbon electrode-based perovskite modules and (**b**) metal-electrode perovskite modules after being stored at room temperature (20–28 °C, 30–60% relative humidity) for five days. Figure S14: Scanning electron microscopy (SEM) cross-sectional images of the C-PSC. Figure S15: Temperature rise behavior of distinct film layer structures under AM1.5G illumination. Figure S16: Temperature rise profiles of (**a**) individual perovskite layers (at ambient temperature of 22 °C) and (**b**) fully integrated C-PSCs (at ambient temperature of 17 °C), along with the corresponding current-voltage (I–V) characteristics of (**c**) fully integrated C-PSCs. Figure S17: Power conversion efficiency (PCE) statistics of the 20 C-PSCs modules. Table S1: Comparison between our results and state-of-the-art solar water splitting systems that have been reported recently. Supplementary Materials 2. References [26–46] are cited in the Supplementary Materials 1.

Author Contributions

K.Z.: conceptualization, methodology, writing—original draft preparation, writing—review and editing; C.Z.: conceptualization, methodology, writing—original draft preparation, writing—review and editing; S.Y.: conceptualization, writing—original draft preparation, writing—review and editing; Z.L.: methodology, investigation; C.L.(Changqing Lin): methodology, investigation; X.W.: methodology; M.J.: writing—reviewing and editing; C.L.(Chunyu Lv): investigation; Y.H.: investigation; W.Z.: investigation, data curation; Q.L.: investigation, data curation; Z.Y.: resources; J.W.: supervision, writing—review and editing; H.C.: supervision. All authors have read and agreed to the published version of the manuscript.

Funding

Institutional Review Board Statement

Not Applicable.

Informed Consent Statement

Not Applicable.

Data Availability Statement

The data that support the findings of this study are available from the corresponding author upon reasonable request.

Conflicts of Interest

The authors declare no conflict of interest. Given the role as Editor-in-Chief, Shihe Yang had no involvement in the peer review of this paper and had no access to information regarding its peer-review process. Full responsibility for the editorial process of this paper was delegated to another editor of the journal.

Use of AI and AI-Assisted Technologies

No AI tools were utilized for this paper.

References

1. Wang, Z.; Song, Z.; Yan, Y.; et al. Perovskite—A Perfect Top Cell for Tandem Devices to Break the S-Q Limit. *Adv. Sci.* **2019**, *6*, 1801704. https://doi.org/10.1002/advs.201801704.
2. Wang, K.; Zheng, L.; Hou, Y.; et al. Overcoming Shockley-Queisser limit using halide perovskite platform? *Joule* **2022**, *6*, 756–771. https://doi.org/10.1016/j.joule.2022.01.009.
3. Zhang, L.; Li, H.; Zhang, K.; et al. Major strategies for improving the performance of perovskite solar cells. *iEnergy* **2023**, *2*, 172–199. https://doi.org/10.23919/IEN.2023.0026.
4. Xu, L.; Xiong, Y.; Mei, A.; et al. Efficient Perovskite Photovoltaic-Thermoelectric Hybrid Device. *Adv. Energy Mater.* **2018**, *8*, 1702937. https://doi.org/10.1002/aenm.201702937.
5. Guo, Q.; Duan, J.; Zhao, Y.; et al. Hybrid Energy Harvesting Solar Cells—From Principles to Applications. *Prog. Chem.* **2023**, *35*, 318–329. https://doi.org/10.7536/pc220706.
6. Li, J.; Duan, J.; Guo, Q.; et al. Accelerating Thermal Transfer in Perovskite Films for High-Efficiency and Stable Photovoltaics. *Adv. Funct. Mater.* **2023**, *33*, 2308036. https://doi.org/10.1002/adfm.202308036.
7. Guo, Q.; Zhao, Y.; Tang, Q.; et al. Heat Management Strategy for All-Inorganic, Full-Spectral Concentrator $CsPbBr_3$/Bi_2Te_3-Integrated Solar Cells. *Sol. RRL* **2022**, *6*, 2200570. https://doi.org/10.1002/solr.202200570.
8. Moot, T.; Patel, J.B.; McAndrews, G.; et al. Temperature Coefficients of Perovskite Photovoltaics for Energy Yield Calculations. *ACS Energy Lett.* **2021**, *6*, 2038–2047. https://doi.org/10.1021/acsenergylett.1c00748.
9. Jošt, M.; Lipovšek, B.; Glažar, B.; et al. Perovskite Solar Cells go Outdoors: Field Testing and Temperature Effects on Energy Yield. *Adv. Energy Mater.* **2020**, *10*, 2000454. https://doi.org/10.1002/aenm.202000454.
10. Ren, Y.; Zhang, K.; Lin, Z.; et al. Long-Chain Gemini Surfactant-Assisted Blade Coating Enables Large-Area Carbon-Based Perovskite Solar Modules with Record Performance. *Nano-Micro Lett.* **2023**, *15*, 182. https://doi.org/10.1007/s40820-023-01155-w.
11. Guillemoles, J.-F.; Kirchartz, T.; Cahen, D.; et al. Guide for the perplexed to the Shockley–Queisser model for solar cells. *Nat. Photonics* **2019**, *13*, 501–505. https://doi.org/10.1038/s41566-019-0479-2.
12. Tobe, T.; Shibayama, N.; Nakamura, Y.; et al. Investigation of the Temperature Coefficients of Perovskite Solar Cells for Application in High-Temperature Environments. *Chem. Asian J.* **2024**, *19*, e202400686. https://doi.org/10.1002/asia.202400686.
13. Tress, W.; Domanski, K.; Carlsen, B.; et al. Performance of perovskite solar cells under simulated temperature-illumination real-world operating conditions. *Nat. Energy* **2019**, *4*, 568–574. https://doi.org/10.1038/s41560-019-0400-8.
14. Babics, M.; Bristow, H.; Pininti, A.R.; et al. Temperature Coefficients of Perovskite/Silicon Tandem Solar Cells. *ACS Energy Lett.* **2023**, *8*, 3013–3015. https://doi.org/10.1021/acsenergylett.3c00930.
15. Shockley, W.; Queisser, H.J. Detailed Balance Limit of Efficiency of p-n Junction Solar Cells. *J. Appl. Phys.* **1961**, *32*, 510–519. https://doi.org/10.1063/1.1736034.
16. Rühle, S. Tabulated values of the Shockley–Queisser limit for single junction solar cells. *Sol. Energy* **2016**, *130*, 139–147. https://doi.org/10.1016/j.solener.2016.02.015.
17. Jia, J.; Seitz, L.C.; Benck, J.D.; et al. Solar water splitting by photovoltaic-electrolysis with a solar-to-hydrogen efficiency over 30%. *Nat. Commun.* **2016**, *7*, 13237. https://doi.org/10.1038/ncomms13237.
18. Ünlü, F.; Florez, A.; Dodd-Clements, K.; et al. Toward Green Processing of Perovskite Solar Cells: Protic Ionic Liquids Enable Water- and Alcohol-Based $MAPbI_3$ Precursors Inks for Slot-Die Coating. *Adv. Energy Mater.* **2025**, *15*, 2403626. https://doi.org/10.1002/aenm.202403626.
19. Liu, S.; Li, J.; Xiao, W.; et al. Buried interface molecular hybrid for inverted perovskite solar cells. *Nature* **2024**, *632*, 536–542. https://doi.org/10.1038/s41586-024-07723-3.
20. Yu, W.; Zou, Y.; Zhang, S.; et al. Carbon-based perovskite solar cells with electron and hole-transporting-blocking layers. *Mater. Futures* **2023**, *2*, 022101. https://doi.org/10.1088/2752-5724/acbbc2.
21. Cui, X.; Ruan, Q.; Zhuo, X.; et al. Photothermal Nanomaterials: A Powerful Light-to-Heat Converter. *Chem. Rev.* **2023**, *123*, 6891–6952. https://doi.org/10.1021/acs.chemrev.3c00159.
22. Balandin, A.A. Thermal properties of graphene and nanostructured carbon materials. *Nat. Mater.* **2011**, *10*, 569–581. https://doi.org/10.1038/nmat3064.
23. Xie, Y.; Wang, X. Thermal conductivity of carbon-based nanomaterials: Deep understanding of the structural effects. *Green Carbon* **2023**, *1*, 47–57. https://doi.org/10.1016/j.greenca.2023.08.004.
24. Liang, Y.; Cui, X.; Li, F.; et al. Minimizing and Controlling Hydrogen for Highly Efficient Formamidinium Lead Triiodide Solar Cells. *J. Am. Chem. Soc.* **2022**, *144*, 6770–6778. https://doi.org/10.1021/jacs.2c00038.

25. Liang, Y.; Cui, X.**;** Li, F.; et al. Trapped-Hydrogen-Induced Energy Loss in Tin-Based Hybrid Perovskite Solar Cells. *Phys. Rev. Appl.* **2022**, *18*, 034084. https://doi.org/10.1103/PhysRevApplied.18.034084.

26. Winterton, R.H.S. Newton's law of cooling. *Contemp. Phys.* **1999**, *40*, 205–212.

27. Tipler, P.A.; Mosca, G. *Physics for Scientists and Engineers: Standard*, 6th ed.; W.H. Freeman: New York, NY, USA, 2008.

28. Landman, A.; Dotan, H.; Shter, G.E.; et al. Photoelectrochemical water splitting in separate oxygen and hydrogen cells. *Nat. Mater.* **2017**, *16*, 646–651.

29. Chen, H.; Song, L.; Ouyang, S.; et al. Co and Fe Codoped $WO_{2.72}$ as Alkaline-Solution-Available Oxygen Evolution Reaction Catalyst to Construct Photovoltaic Water Splitting System with Solar-To-Hydrogen Efficiency of 16.9%. *Adv. Sci.* **2019**, *6*, 1900465.

30. Ekspong, J.; Larsen, C.; Stenberg, J.; et al. Solar-Driven Water Splitting at 13.8% Solar-to-Hydrogen Efficiency by an Earth-Abundant Electrolyzer. *ACS Sustain. Chem. Eng.* **2021**, *9*, 14070–14078.

31. Hansora, D.; Yoo, J.W.; Mehrotra, R.; et al. All-perovskite-based unassisted photoelectrochemical water splitting system for efficient, stable and scalable solar hydrogen production. *Nat. Energy* **2024**, *9*, 272–284.

32. Rhee, R.; Kim, T.G.; Jang, G.Y.; et al. Unassisted overall water splitting with a solar-to-hydrogen efficiency of over 10% by coupled lead halide perovskite photoelectrodes. *Carbon Energy* **2023**, *5*, e232.

33. Nam, Y.; Kim, D.; Chu, J.; et al. Highly Efficient and Stable Iridium Oxygen Evolution Reaction Electrocatalysts Based on Porous Nickel Nanotube Template Enabling Tandem Devices with Solar-to-Hydrogen Conversion Efficiency Exceeding 10%. *Adv. Sci.* **2022**, *9*, 2104938.

34. Li, Y.; Ma, Z.; Hou, S.; et al. Transition metals-based electrocatalysts on super-flat substrate for perovskite photovoltaic hydrogen production with 13.75% solar to hydrogen efficiency. *J. Colloid Interface Sci.* **2025**, *677*, 599–609.

35. Wu, Q.; Guo, J.; Sun, R.; et al. Slot-die printed non-fullerene organic solar cells with the highest efficiency of 12.9% for low-cost PV-driven water splitting. *Nano Energy* **2019**, *61*, 559–566.

36. Liang, J.; Han, X.; Qiu, Y.; et al. A Low-Cost and High-Efficiency Integrated Device toward Solar-Driven Water Splitting. *ACS Nano* **2020**, *14*, 5426–5434.

37. Chen, H.; Zhang, M.; Tran-Phu, T.; et al. Integrating Low-Cost Earth-Abundant Co-Catalysts with Encapsulated Perovskite Solar Cells for Efficient and Stable Overall Solar Water Splitting. *Adv. Funct. Mater.* **2021**, *31*, 2008245.

38. Asiri, A.M.; Ren, D.; Zhang, H.; et al. Solar Water Splitting Using Earth-Abundant Electrocatalysts Driven by High-Efficiency Perovskite Solar Cells. *ChemSusChem* **2022**, *15*, e202102471.

39. Park, J.; Lee, J.; Lee, H.; et al. Hybrid Perovskite-Based Wireless Integrated Device Exceeding a Solar to Hydrogen Conversion Efficiency of 11%. *Small* **2023**, *19*, 2300174.

40. Pan, S.; Li, R.; Wang, J.; et al. Floating Seawater Splitting Device Basedon NiFeCrMo Metal Hydroxide Electrocatalyst and Perovskite/Silicon Tandem Solar Cells. *ACS Nano* **2023**, *17*, 4539–4550.

41. Song, Z.; Li, C.; Chen, L.; et al. All-Perovskite Tandem Photoelectrodes for Unassisted Solar Hydrogen Production. *ACS Energy Lett.* **2023**, *8*, 2611–2619.

42. Fehr, A.M.K.; Agrawal, A.; Mandani, F.; et al. Integrated halide perovskite photoelectrochemical cells with solar-driven water-splitting efficiency of 20.8. *Nat. Commun.* **2023**, *14*, 3797.

43. Wang, J.; Branco, B.; Remmerswaal, W.H.M.; et al. Performance and stability analysis of all-perovskite tandem photovoltaics in light-driven electrochemical water splitting. *Nat. Commun.* **2025**, *16*, 174.

44. Lee, M.; Ding, X.; Banerjee, S.; et al. Bifunctional $CoFeVO_x$ Catalyst for Solar Water Splitting by using Multijunction and Heterojunction Silicon Solar Cells. *Adv. Mater. Technol.* **2020**, *5*, 2000592.

45. Butson, J.D.; Sharma, A.; Tournet, J.; et al. Unlocking Ultra-High Performance in Immersed Solar Water Splitting with Optimised Energetics. *Adv. Energy Mater.* **2023**, *13*, 2301793.

46. Walczak, K.A.; Segev, G.; Larson, D.M.; et al. Hybrid Composite Coatings for Durable and Efficient Solar Hydrogen Generation under Diverse Operating Conditions. *Adv. Energy Mater.* **2017**, *7*, 1602791.